

PAPER

Deriving time-varying cellular motility parameters via wavelet analysis

To cite this article: Yanping Liu *et al* 2021 *Phys. Biol.* **18** 046007

View the [article online](#) for updates and enhancements.



IOP | ebooks™

Bringing together innovative digital publishing with leading authors from the global scientific community.

Start exploring the collection—download the first chapter of every title for free.

Physical Biology



PAPER

Deriving time-varying cellular motility parameters via wavelet analysis

RECEIVED
14 January 2021

REVISED
28 March 2021

ACCEPTED FOR PUBLICATION
28 April 2021

PUBLISHED
9 June 2021

Yanping Liu^{1,9} , Yang Jiao^{2,3,9} , Da He^{4,9}, Qihui Fan⁵, Yu Zheng³, Guoqiang Li¹, Gao Wang¹, Jingru Yao¹, Guo Chen¹, Silong Lou⁶, Jianwei Shuai^{7,8,*} and Liyu Liu^{1,*}

¹ Chongqing Key Laboratory of Soft Condensed Matter Physics and Smart Materials, College of Physics, Chongqing University, Chongqing, 401331, People's Republic of China

² Materials Science and Engineering, Arizona State University, Tempe, Arizona 85287, United States of America

³ Department of Physics, Arizona State University, Tempe, Arizona 85287, United States of America

⁴ Spine Surgery, Beijing Jishuitan Hospital, Beijing, 100035, People's Republic of China

⁵ Beijing National Laboratory for Condensed Matter Physics and CAS Key Laboratory of Soft Matter Physics, Institute of Physics, Chinese Academy of Sciences, Beijing 100190, People's Republic of China

⁶ Department of Neurosurgery, Chongqing University Cancer Hospital, Chongqing, 400030, People's Republic of China

⁷ Department of Physics and Fujian Provincial Key Laboratory for Soft Functional Materials Research, Xiamen University, Xiamen 361005, People's Republic of China

⁸ Wenzhou Institute, University of Chinese Academy of Sciences, Wenzhou 325000, People's Republic of China

⁹ These authors contributed equally to this work.

* Authors to whom any correspondence should be addressed.

E-mail: jianweishuai@xmu.edu.cn and lyliu@cqu.edu.cn

Keywords: cell migration, time-varying characteristics, motility parameter, wavelet transform, complex microenvironment

Abstract

Cell migration, which is regulated by intracellular signaling pathways (ICSP) and extracellular matrix (ECM), plays an indispensable role in many physiological and pathological process such as normal tissue development and cancer metastasis. However, there is a lack of rigorous and quantitative tools for analyzing the time-varying characteristics of cell migration in heterogeneous microenvironment, resulted from, e.g. the time-dependent local stiffness due to microstructural remodeling by migrating cells. Here, we develop a wavelet-analysis approach to derive the time-dependent motility parameters from cell migration trajectories, based on the time-varying persistent random walk model. In particular, the wavelet denoising and wavelet transform are employed to analyze migration velocities and obtain the wavelet power spectrum. Subsequently, the time-dependent motility parameters are derived via Lorentzian power spectrum. Our results based on synthetic data indicate the superiority of the method for estimating the intrinsic transient motility parameters, robust against a variety of stochastic noises. We also carry out a systematic parameter study and elaborate the effects of parameter selection on the performance of the method. Moreover, we demonstrate the utility of our approach via analyzing experimental data of *in vitro* cell migration in distinct microenvironments, including the migration of MDA-MB-231 cells in confined micro-channel arrays and correlated migration of MCF-10A cells due to ECM-mediated mechanical coupling. Our analysis shows that our approach can be as a powerful tool to accurately derive the time-dependent motility parameters, and further analyze the time-dependent characteristics of cell migration regulated by complex microenvironment.

1. Introduction

Cell migration [1] is a ubiquitous and basic biological phenomenon that underlies many crucial physiological processes for normal tissue and organ development as well as immunological responses [2], wound healing [3], embryogenesis [4]. Eukaryotic cell migration is a complex process involving many cellular and sub-cellular level events [5], which are regulated by

various intracellular signaling pathways (ICSP) [6] and the extracellular matrix (ECM) [7, 8]. The onset of ill-regulated cell migration is often associated with many human diseases, and the most representative example is cancer metastasis [9, 10].

In order to study cell behaviors, a number of interesting works have been done in recent years. It was reported that the substrates with different rigidities lead to different cell movements, namely

stiffer substrates generally promote the directionality of cell movement, while soft substrates typically result in random motions [11]. These distinct behaviors regulated by substrate stiffness are called ‘durotaxis’, which are combined with mechanical strains to control a number of pathological processes involving cell migration [12]. In addition to substrates, the gradient of the nanoscale topographic features in ECM will guide a new type of directed migration termed as ‘topotaxis’ and the direction of topotaxis can reflect the effective cell stiffness [13]. Furthermore, in order to systematically investigate the heterogeneous ECM, a micro-fabricated biochip was constructed to create a 3D funnel-like matrigel interface, which verified that the heterogeneous structures of ECM can guide the aggressive cell invasion in the rigid matrigel space [14]. More recently, it was shown that the local fiber alignment in a constructed collagen I-matrigel microenvironment directs the migration of MDA-MB-231 breast cancer cells during the intravasation into rigid matrigel [15].

To phenomenologically describe the anisotropic migratory behaviors, a persistent random walk model (PRW) [16–18] has been proposed, which explicitly considers the memory of cell to the past velocities. The PRW model is based on Brownian motion [19], and can be derived from Langevin equation [20] of the following form

$$\frac{d\vec{v}}{dt} = -\frac{\vec{v}}{P} + \frac{S}{\sqrt{P}} \cdot \tilde{w}, \quad (1)$$

where \vec{v} is the migration velocity, P is the persistence time, S is the averaged migration speed and \tilde{w} is the random vector of a Wiener process [21]. Note that neither of the parameters P and S change with time in PRW model. Inspired by the PRW model, many novel models have been constructed for exploring how cells behave in complex ECM [22]. For example, amoeba exhibits a special random walk mode, which can greatly increase the chance of finding a target [23]. Likewise, CD8 (+) T cell in brain performs a movement known as generalized Lévy walk, which enables T cells to find rare targets [24]. Moreover, a mathematical model was developed for describing the statistical properties of cell’s velocity and centroid, which are consistent with the phenomenological description of amoeboid motility [25].

In the study of cellular phenomena and modeling cell movements, accurately characterizing cell migration capability is of great interest. In order to address the challenge that the total time of the recorded trajectories in the experiments may not be precisely controlled, an optimal estimation was constructed to obtain the diffusion coefficients based on the individual and short trajectories [26]. Similarly, an unbiased and practically optimal covariance-based estimator was also constructed to optimally determine the diffusion coefficient of a diffusing particle

from a time-lapse recorded trajectory [27]. Besides the diffusion coefficient, the direction autocorrelation function and other essential quantities are computed to analyze cell migration in two dimensions, based on an open-source computer program, DiPer [28]. In the previous works, we also developed exclusive methods to analyze anisotropic ECM and derived the time-independent cellular motility parameters [29, 30].

Different from the cases above whose characteristics and properties are assumed to be non-varying with time, the more complex ECM changes globally or locally due to the changes of temperature, pressure, the heterogeneous surfaces in which cells migrate [11, 12], the special components (oriented fibers) [15] or the concentration of biochemical factors [7] such as cytokine or drug molecules. In addition, migrating cells can actively remodel the ECM either mechanically or chemically, leading to spatial-temporally varying properties that in turn influences cell migration [31–33]. Accordingly, there are a few works focusing on time-varying cell dynamics in heterogeneous ECM. For instance, when cells migrate on the tissue with cultured polystyrene surface, a random motion coefficient increased significantly over time, while for experiments with untreated polystyrene plates, the random motion coefficient remained relatively constant [34].

In this study, we consider the PRW in ECM with time-varying characteristics, and propose an approach to derive the time-dependent motility parameters (persistence time and migration speed) from cell migration trajectories. Specifically, we introduce wavelet transform (WT) to analyze the cell migration velocities and obtain the wavelet power spectrum, which exhibits the time-frequency characteristics of cell trajectories. Moreover, the time-dependent motility parameters can be derived from the fits to wavelet power spectrum at each moment with Lorentzian power spectrum (LPS), and we introduce wavelet denoising (WD) on migration velocities to derive more accurate motility parameters before performing the WT. Finally, we also validate the utility of our approach by analyzing experimental data of *in vitro* cell migration regulated by complex microenvironment.

The rest of the paper is organized as follows: in section 2, we introduce the PRW model in ECM with time-varying characteristics, further explore the properties of cell migration and illustrate the limitations of commonly used physical quantities for characterizing cellular dynamics in a certain situation. In section 3, we combine the WD, WT with LPS to derive the time-dependent motility parameters, and demonstrate the utility of the proposed approach via representative examples. We also analyze the effects of several factors on the performance of the approach, and clarify the limitations of our approach.

In section 4, we employ our approach to analyze the time-dependent characteristics of *in vitro* cell migration, and reveal the underlying mechanism of the highly correlated cell pair. In section 5, we provide concluding remarks.

2. Persistent random walk model with time-varying motility parameters

In this section, we develop a motility model to describe cell dynamics in ECM with time-varying characteristics. Based on the model, we computationally generate cell migration trajectories. The analysis of these trajectories shows that commonly used classic physical quantities, including mean squared displacement (MSD), velocity autocovariance function (VAC) and Fourier power spectrum (FPS), are not sufficient to characterize cell motility.

2.1. The effects of ICSP/ECM with time-varying characteristics on cell motility

Inspired by the time-varying protein content, e.g. Arpin [6], physical/chemical properties, we generalize the classical PRW [16–18] and obtain a new motility model, namely the time-varying persistent random walk model (TPRW). Note that both the parameters P and S in this model are varying with time, which together quantify the time-dependent cell migration capability.

For simplicity, we first construct the following affine functions for P and S [11], written as

$$P(t) = K_P \cdot t + P_0, \quad (2)$$

$$S(t) = K_S \cdot t + S_0, \quad (3)$$

where the constant P_0 and S_0 are motility parameters at $t = 0$. K_P and K_S are coefficients quantifying the changing rates of motility parameters P and S . The functions defined above indicate that the cellular migration capability gradually changes linearly with time, and further reflect the effects of ICSP/ECM on cell motility.

2.2. Numerical simulation of cell migration trajectories

In order to explore the characteristics of cell migration trajectories, we first specify the parameters in time-dependent functions in equations (2) and (3), i.e. $K_P = 7.292 \times 10^{-4}$, $P_0 = 0.3$ min, $K_S = 2.083 \times 10^{-4}$ $\mu\text{m min}^{-2}$ and $S_0 = 0.1 \mu\text{m min}^{-1}$. Here, the values of parameters are defined by referring the work [35], partly. Thus, the motility parameter P lies in the interval of 0.3–1.0 min, while S in the interval of 0.1–0.3 $\mu\text{m min}^{-1}$, as plotted in figure 1(a). Cell trajectories can be then simulated by TPRW model according to equations (4)–(9). In particular, the cell position at each time step can be obtained easily according to the following equations [30, 36]

$$x(t + \Delta t) = x(t) + \Delta x(t, \Delta t), \quad (4)$$

$$y(t + \Delta t) = y(t) + \Delta y(t, \Delta t), \quad (5)$$

here Δx and Δy are displacements of cell position in x and y axes in the time step size of Δt . Further, the displacements are given by

$$\Delta x(t, \Delta t) = \alpha(t) \cdot \Delta x(t - \Delta t, \Delta t) + F(t) \cdot W, \quad (6)$$

$$\Delta y(t, \Delta t) = \alpha(t) \cdot \Delta y(t - \Delta t, \Delta t) + F(t) \cdot W, \quad (7)$$

where $\alpha(t) = 1 - \Delta t/P(t)$ and $F(t) = \sqrt{S(t)^2 \cdot \Delta t^3/P(t)}$. The former denotes the memory of cell to the past velocities, while the latter is noise amplitude. $W \sim N(0, 1)$ is white noise. Note that the values of P are not less than that of Δt , ensuring that α is always greater than zero. In computer simulations, the total recording time T is 960 min and the time step size Δt is 0.2 min. At the two limits of persistence time, the cell migration described by TPRW model either becomes the ballistic motion ($P \sim \infty$) or the random walk ($P \sim \Delta t$). In order to mimic the uncertainties in experimental observations, we further add the positioning errors σ_{pos} to the simulated trajectories by

$$\hat{x}(t) = x(t) + \sigma_{\text{pos}} \cdot W, \quad (8)$$

$$\hat{y}(t) = y(t) + \sigma_{\text{pos}} \cdot W, \quad (9)$$

where σ_{pos} is set as 0.01 μm [17]. We simulate 200 independent cell migration trajectories, and a representative trajectory is presented in figure 1(b).

For each trajectory, the migration velocities are computed based on the displacements within the time step Δt . The velocities in figure 1(c) gradually increase with time, which is the consequence of motility parameters in figure 1(a). Moreover, the square of velocities obeys an exponential decay in lin–log axes [see figure 1(d)], which may indicate that velocity still are Gaussian distributed [35]. Based on the computed migration velocities, we also obtain the angle displacements between any two successive velocity vectors. The corresponding distribution is presented in figure 1(e), which are symmetric at 0 rad in the interval of $(-\pi, \pi)$ and means that the chances of turning left and right are identical when cell migrates. Moreover, the distribution indicates that a self-propelled cell prefers to migrate along a fixed direction, instead of a large deflection. In addition, migration velocities become smaller when the corresponding angle displacements increase as depicted in figure 1(f). These results indicate that a high-speed moving cell tends to migrate in straight line, while a low-speed cell tends to make turn. The phenomenon is also investigated in references [25, 37]. These aspects indicate the TPRW model are consistent with the Ornstein–Uhlenbeck process (OU) [38] to some extent, and we believe that the TPRW model could be regarded as the superposition of many OU models.

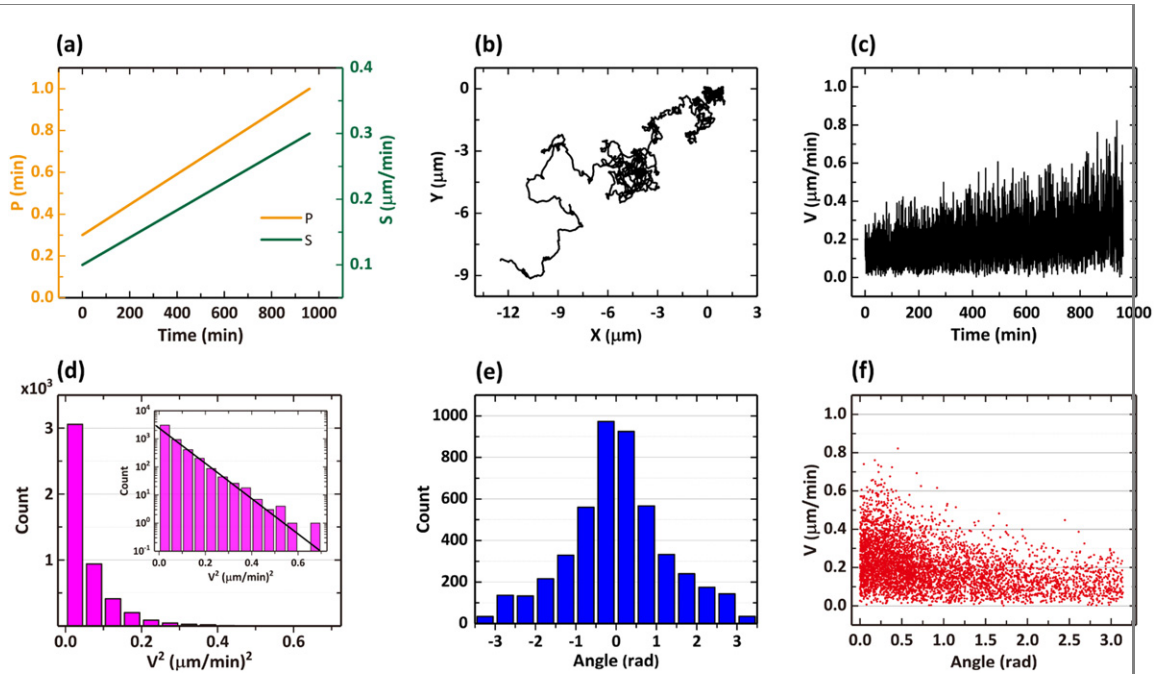


Figure 1. The PRW model with time-varying motility parameters (TPRW model). (a) The linearly time-dependent functions [cf equations (2) and (3)] of motility parameters. The orange line corresponds to the persistence time P , while the green line corresponds to the migration speed S . (b) Individual cell migration trajectories consisting of $4800 + 1 (N + 1)$ frames simulated by TPRW model. (c) Cell migration velocities plotted against time. (d) Distribution of the square of cell migration velocities. The inset indicates the same histogram but in lin–log axes and the black straight line denotes an exponential decay. (e) Distribution of the angles between any two successive velocities. (f) Cell migration velocities as functions of angles between any two successive velocities.

2.3. Characterizing cell migration

In what follows, we employ three classical physical quantities, including the MSD, VAC function, and FPS to investigate the overall averaged motility parameters P and S . We illustrate the limitations of the three quantities when extracting the time-dependent motility parameters.

2.3.1. Mean squared displacement

First we calculate the MSD [28, 35, 39] based on the coordinates of cell migration trajectory $\vec{r}_{i \cdot \Delta t}$ ($i = 0, \dots, N$) in Cartesian coordinates given by

$$\text{MSD}(n \cdot \Delta t) = \frac{1}{N - n + 1} \sum_{i=0}^{N-n} (\vec{r}_{(i+n) \cdot \Delta t} - \vec{r}_{i \cdot \Delta t})^2, \quad (10)$$

where \vec{r} is the position vector of individual cells at each time step, N the total number of displacements per trajectory, n the step size. The overall averaged MSD for 200 simulated trajectories is plotted in figure 2(a). Here the theoretical MSD [28, 36] reads as

$$\text{MSD}(t) = 4D \cdot (t - P + P \cdot e^{-t/P}) + 4\sigma_{\text{pos}}^2, \quad (11)$$

where D is the diffusion coefficient. Therefore, we obtain a set of motility parameters P , D and σ_{pos} by the fit to the overall averaged MSD, and the migration speed S is computed by the following formula [29, 34]

$$S = \sqrt{\frac{2D}{P}}. \quad (12)$$

The resulting parameters are shown in figures 2(d)–(f).

2.3.2. Velocity autocovariance function

Similarly, figure 2(b) shows the overall averaged VAC function, in which the VAC for individual trajectories is computed by [17]

$$\begin{aligned} \text{VAC}(n \cdot \Delta t) &= \langle \vec{v}_{i \cdot \Delta t} \cdot \vec{v}_{(i+n) \cdot \Delta t} \rangle \\ &= \frac{1}{N - n - 1} \\ &\times \sum_{k=1}^{N-n} \left(\vec{v}_{k \cdot \Delta t} - \frac{1}{N - n} \sum_{l=1}^{N-n} \vec{v}_{l \cdot \Delta t} \right) \\ &\times \left(\vec{v}_{(k+n) \cdot \Delta t} - \frac{1}{N - n} \sum_{l=n+1}^N \vec{v}_{l \cdot \Delta t} \right). \quad (13) \end{aligned}$$

After computing the VAC based on cell migration velocities, a widely-used fit can be performed via a revised exponential decay, which is given as [35]

$$\text{VAC}_j = \text{VAC}_j^{(\text{true})} \quad \text{for } |j| \geq 2, \quad (14)$$

$$\text{VAC}_{\pm 1} = \text{VAC}_1^{(\text{true})} - 2\sigma_{\text{pos}}^2/(\Delta t)^2, \quad (15)$$

$$\text{VAC}_0 = \text{VAC}_0^{(\text{true})} + 4\sigma_{\text{pos}}^2/(\Delta t)^2. \quad (16)$$

Note that the theoretical VAC only is affected at times $t_0 = 0$ and $t_{\pm 1} = \pm \Delta t$ when considering the

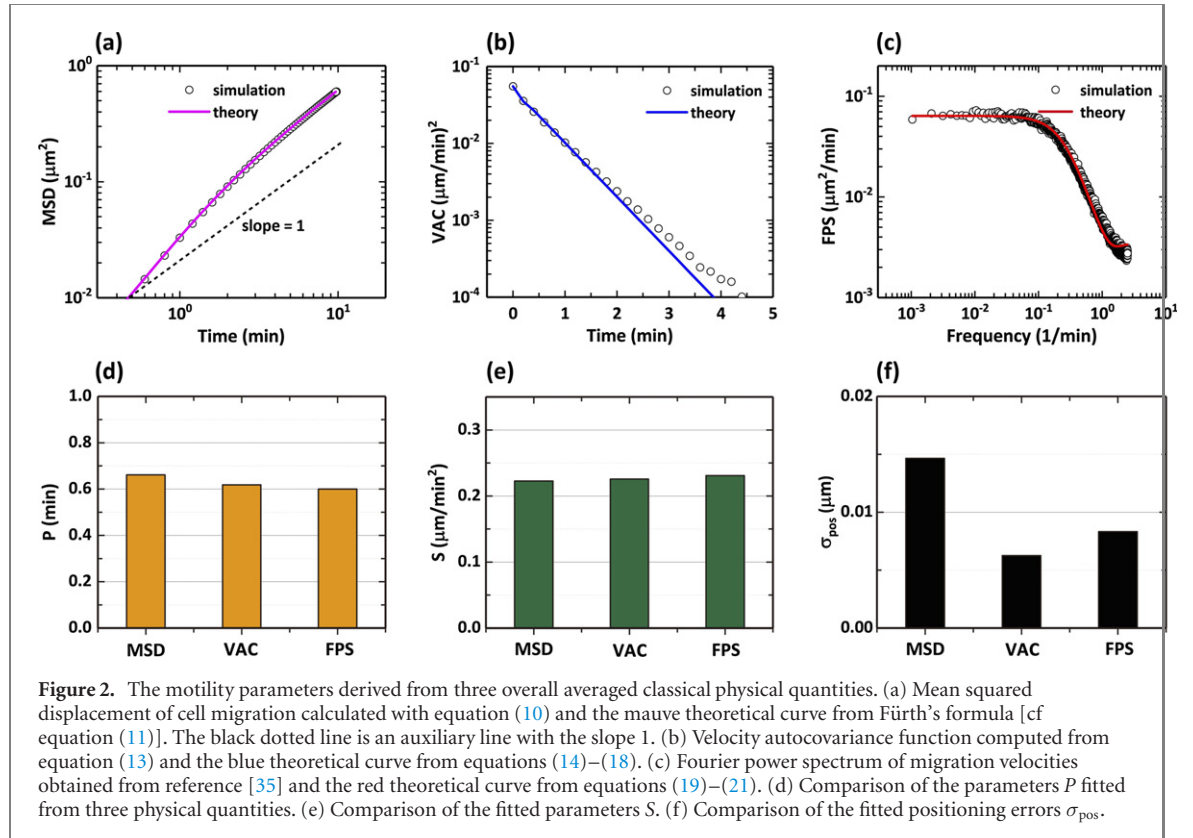


Figure 2. The motility parameters derived from three overall averaged classical physical quantities. (a) Mean squared displacement of cell migration calculated with equation (10) and the mauve theoretical curve from Fürth's formula [cf equation (11)]. The black dotted line is an auxiliary line with the slope 1. (b) Velocity autocovariance function computed from equation (13) and the blue theoretical curve from equations (14)–(18). (c) Fourier power spectrum of migration velocities obtained from reference [35] and the red theoretical curve from equations (19)–(21). (d) Comparison of the parameters P fitted from three physical quantities. (e) Comparison of the fitted parameters S . (f) Comparison of the fitted positioning errors σ_{pos} .

positioning errors. Among the equations above, the $\text{VAC}^{(\text{true})}$ is defined by

$$\text{VAC}_{j-k}^{(\text{true})} = \frac{2P^2 \cdot [\cosh(\Delta t/P) - 1]}{(\Delta t)^2} \times \text{VAC}(t_j - t_k) \quad \text{for } j \neq k, \quad (17)$$

$$\text{VAC}_0^{(\text{true})} = \frac{2P^2 \cdot (e^{-\Delta t/P} - 1 + \Delta t/P)}{(\Delta t)^2} \times \text{VAC}(0) \quad \text{for } j = k. \quad (18)$$

It is evident that the overall averaged VAC in lin-log axes could not be nicely fitted by the revised exponential decay [see figure 2(b)], indicating the insufficiency of the revised exponential decay in analysis of cell migration simulated by TPRW model.

2.3.3. Lorentzian velocity power spectrum

It has been reported that the physical quantities used above could not return reliable errors on the fitted parameters P and S because of the correlations between the velocities [35]. Therefore, another method has been suggested to transform the time domain to frequency domain by performing Fourier transform (FT) of the VAC according to Wiener–Khinchin theorem [40, 41], which can eliminate the correlations. The results are referred to as FPS, as seen in figure 2(c). It behaves like that for PRW model in ECM with temporally non-varying properties. Then we fit the FPS with the LPS of OU process [35], which is defined as

$$\text{LPS}_u(f_k) = \text{LPS}_u^{(\text{true})}(f_k)$$

$$+ \frac{4\sigma_{\text{pos}}^2}{\Delta t} [1 - \cos(\pi \cdot f_k / f_{\text{Nyq}})], \quad (19)$$

where the first term on the right side of equation (19) is the true expression of LPS, with the following form

$$\text{LPS}_u^{(\text{true})}(f_k) = \frac{(1 - c^2)}{c} \cdot \left(\frac{P}{\Delta t} \right)^2 \cdot \text{LPS}_v^{(\text{aliased})}(f_k) + 4D \cdot \left(1 - \frac{1 - c^2}{2c} \cdot \frac{P}{\Delta t} \right), \quad (20)$$

in which the term $\text{LPS}_v^{(\text{aliased})}(f_k)$ is defined by

$$\begin{aligned} \text{LPS}_v^{(\text{aliased})}(f_k) &= \frac{\left\langle \left| \hat{\vec{v}} \right|^2 \right\rangle}{t_{\text{msr}}} \\ &= \frac{(1 - c^2) \cdot 2D \cdot \Delta t / P}{1 + c^2 - 2c \cdot \cos(\pi \cdot f_k / f_{\text{Nyq}})}, \end{aligned} \quad (21)$$

and the second term on the right side of equation (19) is an additional noise term when considering the effect of positioning noise. Here, $c = \exp(-\Delta t/P)$, $f_k = k \cdot \Delta f (k = 1, \dots, N/2)$, $\Delta f = 1/t_{\text{msr}}$, $t_{\text{msr}} = N \cdot \Delta t$ and $f_{\text{Nyq}} = 1/(2 \cdot \Delta t)$. The imperfect fit in high frequency domain (~ 1.0 min) indicates that the LPS is not the most suitable estimator for the FPS.

Figures 2(d)–(f) exhibit the fitted motility parameters P , S and σ_{pos} obtained from overall averaged MSD, VAC and FPS. Figure 2(d) indicates that all the fitted parameters P locate in the interval of

0.6–0.7 min, while the fitted parameters S in the interval of 0.2–0.25 $\mu\text{m min}^{-1}$. Neither of the resulting parameters P and S reflects the corresponding linear functional form of these parameters, they only approximately derive the corresponding averaged values ($P_{\text{ave}} = 0.65 \text{ min}$, $S_{\text{ave}} = 0.2 \mu\text{m min}^{-1}$) of all theoretical P and S , respectively. The positioning error σ_{pos} is independent of the intrinsic characteristics of cell motility and could be regarded as a constant, thus it is reasonable to average the fitted values from MSD and FPS to obtain an approximate positioning error ($\sim 0.11 \mu\text{m}$).

3. Deriving accurately the time-varying motility parameters

In this part, we introduce WT and WD to compute the wavelet power spectra of cell migration velocities, and further derive accurately time-dependent motility parameters via LPS.

3.1. Wavelet transform of migration velocities

The WT was initially employed by Morlet *et al* to analyze seismic signals in the early 1980s [42, 43], and was later formalized by Goupillaud and Grossmann *et al* [44, 45]. Different from the stationary process analyzed by FT, the WT is regarded as a powerful tool to deal with the non-stationary and infinitely correlated process. For example, although the fractional Brownian motion is nonstationary and infinitely correlated, the corresponding wavelet coefficients are stationary and uncorrelated [46]. Kumar *et al* also validated the incapability of FT to characterize the time-varying signals [47]. Further, windowed Fourier transform (WFT) can be computed by performing a sliding window of a constant time interval from a time series. It is also an analysis tool for extracting time-frequency information from a time series, but shows the inaccuracy and inefficiency because of the ‘imposed’ window size into analysis, i.e. how to determine the most appropriate window size and how to address the aliasing of high- and low-frequency, etc, as discussed by Kaiser *et al* [48], Torrence *et al* [49] and Daubechies [50].

Different from the WFT, the window size varies over the frequency in WT, which is the main advantage to analyze the local characteristics of time series [49–51]. The WT includes discrete WT (DWT) and continuous WT (CWT), the latter is utilized in this study. For a given time series v_n , the CWT is defined as the convolution of $v_{n'}$ with a scaled and translated version of the wavelet function $\psi_0(\eta)$, as follows [49]

$$W_n(s) = \sum_{n'=0}^{N-1} v_{n'} \cdot \psi_0^* \left[\frac{(n' - n) \cdot \Delta t}{s} \right], \quad (22)$$

where the symbol $(*)$ denotes the complex conjugate, s is wavelet scale that can result in the compressed/stretched wavelets corresponding to the

high/low Fourier frequency [49]. The wavelet function used here is Morlet, which consists of a plane wave modulated by a Gaussian

$$\psi_0(\eta) = \pi^{-1/4} \cdot e^{i\omega_0 n} \cdot e^{-\eta^2/2}, \quad (23)$$

where ω_0 is the non-dimensional frequency and is set as 6 for satisfying the admissibility condition, which ensures that continuous WT is invertible [52]. The Morlet function used above is complex, so the resulting wavelet coefficient $W_n(s)$ is also complex. Thus, one can gain easily the information about the real part, imaginary part, and finally the wavelet power spectrum is computed by the absolute value squared of the WT [49, 53], i.e. $|W_n(s)|^2$.

So far, one can follow the procedure above to graphically illustrate how the power spectral values change over the frequency and time, as shown in figure 3(a). In figure 3(a), the amplitude of wavelet power spectrum lies in the interval 0 – $0.16 \mu\text{m}^2 \text{ min}^{-1}$ denoted by different colors, which is correlated with the effective diffusion coefficient for a migrating cell at each moment. At the same time, edge effects will occur in the beginning and end of the wavelet power spectrum because of the finite-length time series, which is also called cone of influence (COI) [49], see the sharp decline parts affected by COI in figure 3(b). Note that we do not exclude the sharp decline parts for exhibiting the entire performance of the approach developed.

3.2. Fitting local wavelet power spectra with Lorentzian velocity power spectrum

There is an evident peak with the time increasing in the low-frequency domain [see figure 3(a)], and it corresponds to the linear functions [see figure 1(a)]. Figure 3(a) not only shows the dominant features of migration velocities, but also how these features vary with time. The power spectra along frequency-axis for every moment in figure 3(a) are called local wavelet power spectra, which are identical to the Fourier power spectra of the univariate lag-1 autoregressive [AR(1) or Markov] process, on average [49, 54]. When taking average on wavelet power spectra along frequency-axis, the frequency-averaged power (energy) is obtained, as shown in figure 3(b). The frequency-averaged power behaves like the peak in figure 3(a) and the tendency in figure 1(a), which means that the power of migrating cells increases with time, because of the enhancement of ICSP/ECM. The abnormal decreases in the beginning and the end of the time series are consequences of COI. When the average is taking over all the local wavelet power spectra, one will obtain the global wavelet power spectrum [see figure 3(c)], which is an unbiased and reliable estimation of the true power spectrum of any time series [55].

Further, Torrence *et al* also validated the global wavelet power spectrum approximates to the corresponding FPS [49], thus it is reasonable to

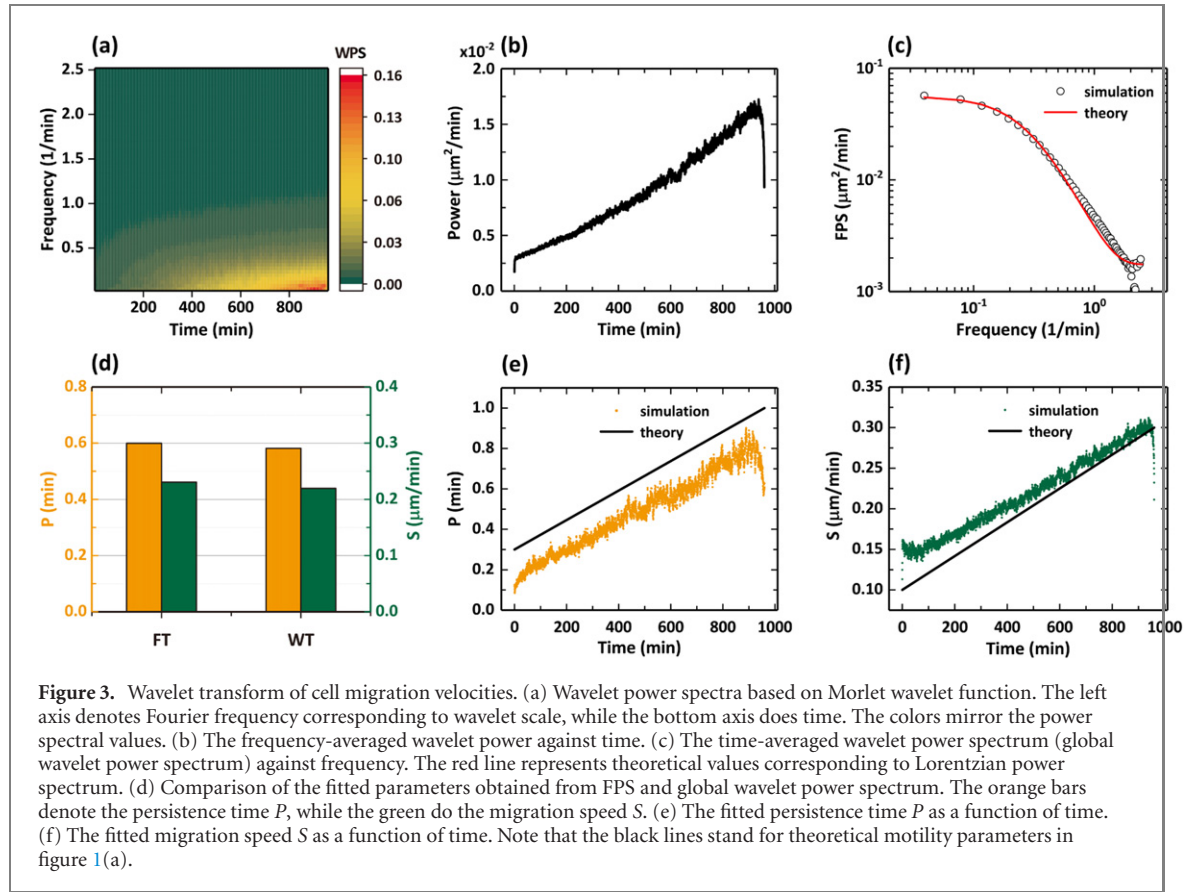


Figure 3. Wavelet transform of cell migration velocities. (a) Wavelet power spectra based on Morlet wavelet function. The left axis denotes Fourier frequency corresponding to wavelet scale, while the bottom axis does time. The colors mirror the power spectral values. (b) The frequency-averaged wavelet power against time. (c) The time-averaged wavelet power spectrum (global wavelet power spectrum) against frequency. The red line represents theoretical values corresponding to Lorentzian power spectrum. (d) Comparison of the fitted parameters obtained from FPS and global wavelet power spectrum. The orange bars denote the persistence time P , while the green do the migration speed S . (e) The fitted persistence time P as a function of time. (f) The fitted migration speed S as a function of time. Note that the black lines stand for theoretical motility parameters in figure 1(a).

fit the global wavelet power spectrum using LPS mentioned in section 2, as shown by black line in figure 3(c). Figure 3(d) displays comparisons between motility parameters fitted from FPS and global wavelet power spectrum, respectively. It is obvious that the fitted parameters P and S based on WT are almost identical to these values based on FT, respectively. These identities further illustrate the rationality of LPS in fitting local wavelet power spectra.

There is no doubt that fitting the local wavelet power spectra using LPS will recover the time-dependent functions [see figures 3(e) and (f)]. The fitted parameters given in figure 3(e) for P and in figure 3(f) for S both encode the linear functions but with large deviations. Here, the fitted positioning errors are not shown due to the experimental observation, because they are not intrinsic terms related to cell motility. The corresponding errors can be estimated based on the results in figure 2(d).

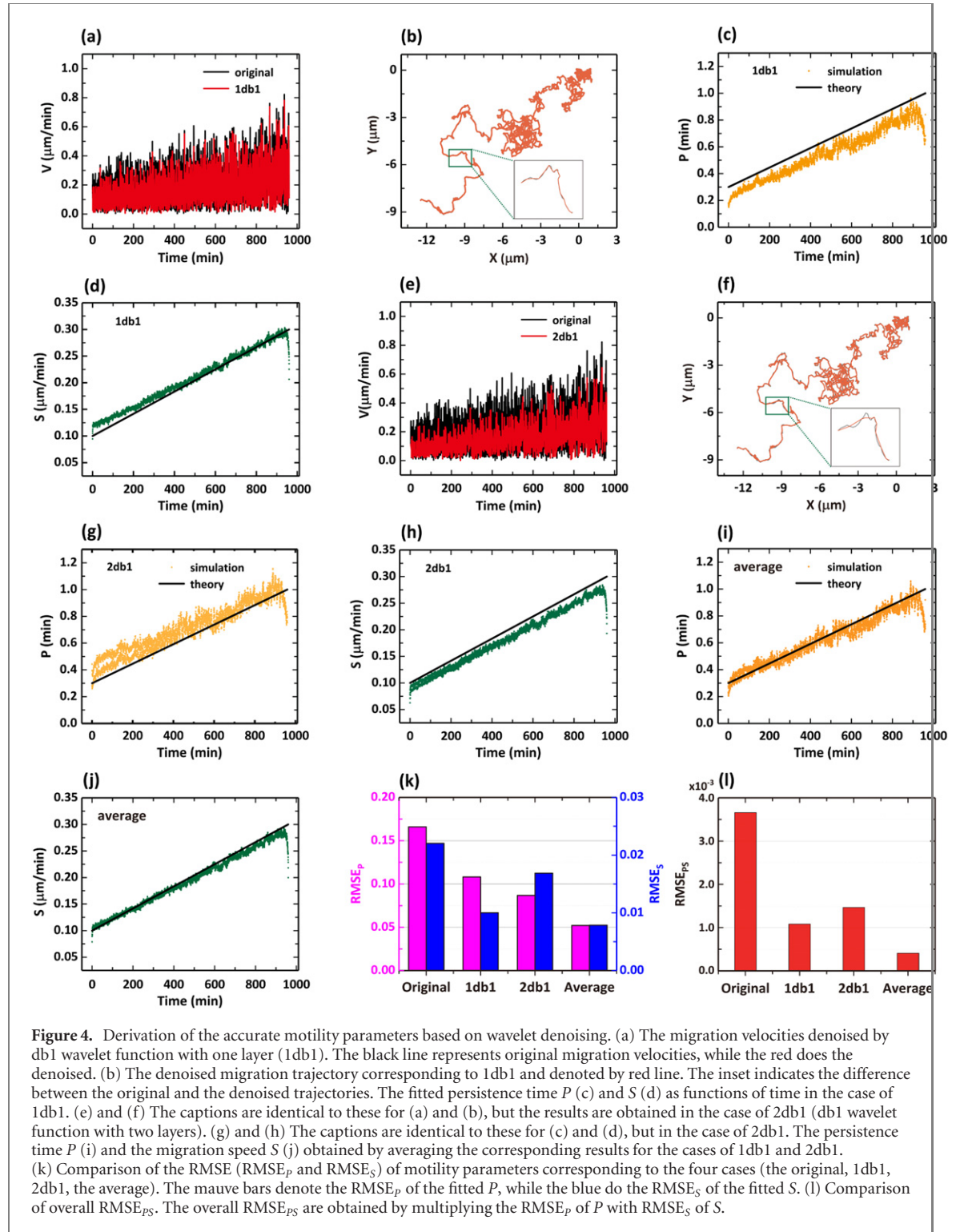
3.3. Wavelet denoising of migration velocities

In this part, we apply the WD to filter the migration velocities before implementing the WT for improving the accuracy of fitting parameters, which involves wavelet decomposition and reconstruction [56, 57]. The calculation program mainly calls some built-in functions (Matlab

R2017a, USA), e.g. `idwt`, `wavedec`, `ddencmp` and `wdencmp`.

First, we decompose the velocities to obtain the wavelet coefficients using Mallet algorithm [57]. Second, the coefficients are automatically thresholded by the program. Then, the thresholded coefficients are reconstructed to obtain the denoised signal, as exhibited in figures 4(a) and (e). Here, the WD used is implemented based on Haar wavelet (also referred to as ‘db1’ in Matlab), which is the only discontinuous one of Daubechies wavelet family and known as the first order Daubechies wavelet db1, see more details in reference [58]. Moreover, the Haar wavelets are most commonly used wavelets in database literature because they are easy to comprehend and fast to compute [59, 60], for instance, denoising the observed data without removing localized significant changes to represent the time-series evolution [61]. When performing the wavelet decomposition once, the process is termed as ‘one layer’ decomposition, while decomposition twice as ‘two layers’. For simplicity, we use ‘1db1’ to represent the process of denoising applying db1 wavelet with ‘one layer’, while ‘2db1’ to represent that with ‘two layers’.

Figure 4(a) compares the original velocities and denoised velocities based on 1db1, which clearly shows the amplitude of the former is generally greater than that of the latter. Furthermore, the corresponding trajectories are exhibited in figure 4(b).



The enlarged inset illustrates the effect of 1db1 on trajectory, and the processed trajectory seems like more smoothly. Likewise, we employ 2db1 to denoise the same original velocities, and the results are shown in figures 4(e) and (f). Comparing the denoised velocities in figures 4(a) and (e), it is evident that the 2db1 filters more velocity components (not just noise). Thus, the 2db1 smooth the trajectory more greatly, as shown by inset in figure 4(f). Note that cell migration trajectories discussed here contains typically two kind of noises,

i.e. errors of observation and intrinsic part of their dynamics [26].

For the migration velocities denoised by 1db1, we follow the same procedure used above, namely fitting local wavelet power spectra with LPS, to derive time-varying motility parameters P and S . The resulting parameters are plotted in figures 4(c) and (d), indicating P and S , respectively. The results for 1db1 are more accurate than these for original velocities in figures 3(e) and (f), which directly highlights the necessary of denoising. More importantly, we find

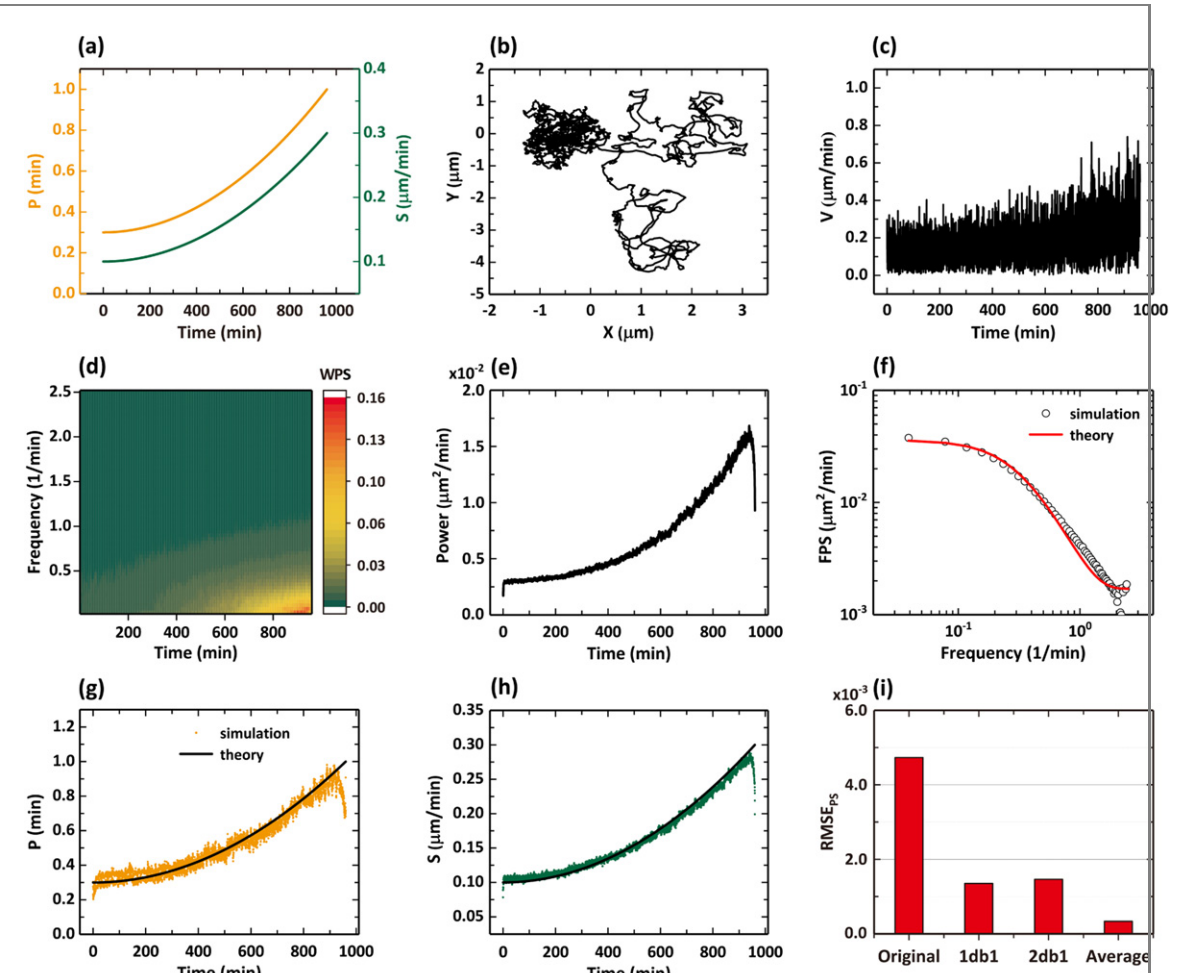


Figure 5. Application of WDTL in deriving the accurate motility parameters following the quadratic functions. The captions are identical with those in figures 1, 3 and 4.

that the fitted P are generally less than theoretical P , while the fitted S greater than theoretical S . we guess this ‘less and great’ is the consequence of insufficient denoising, that is, the velocities denoised by 1db1 still contain some noise components, which decrease the persistence of cell migration. Next, we repeat the procedure but employing 2db1 to derive the motility parameters, as exhibited in figures 4(g) and (h). The results for 2db1 also are more close to theoretical values, but display opposite ‘great and less’. Thus, we argue that the 2db1 is so ‘powerful’ that more velocity components are filtered. This excessive denoising contributes to more persistent cell migration. We further average these corresponding fitted parameters for 1db1 and 2db1, the averaged P and S are plotted in figures 4(i) and (j), respectively. The averaged results are more accurate than these for the original, 1db1 and 2db1. What’s more, the averaged results almost mirror the linear functions.

In order to compare the accuracy of the fitted parameters P and S based on different denoising methods, respectively, the corresponding root mean square errors (RMSE_P and RMSE_S) of the fitted parameters P and S are calculated independently, as seen in figure 4(k). The bars indicate that both the

1db1 and 2db1 are better than the original, but the average is better than 1db1 and 2db1. To be more intuitive, overall RMSE_{PS} are computed by multiplying RMSE (RMSE_P and RMSE_S) of the fitted P and S [see figure 4(l)], and it validates directly the advantage of the average in improving the accuracy of fitting motility parameters. Since the procedure used above mainly involves WD, WT and LPS, we abbreviate it as ‘WDTL’ for simplicity.

3.4. Two examples of ICSP/ECM with time-varying characteristics

3.4.1. Dependency defined by quadratic functions

In the following, we discuss another two time-dependent functions to illustrate the universality of WDTL developed above. The functions for the first example are defined as

$$P(t) = K_P \cdot t^2 + P_0, \quad (24)$$

$$S(t) = K_S \cdot t^2 + S_0, \quad (25)$$

which are graphically shown in figure 5(a).

Next, the corresponding quantities for original migration velocities are computed and plotted in figures 5(b)–(f). They are comparable with figures 1

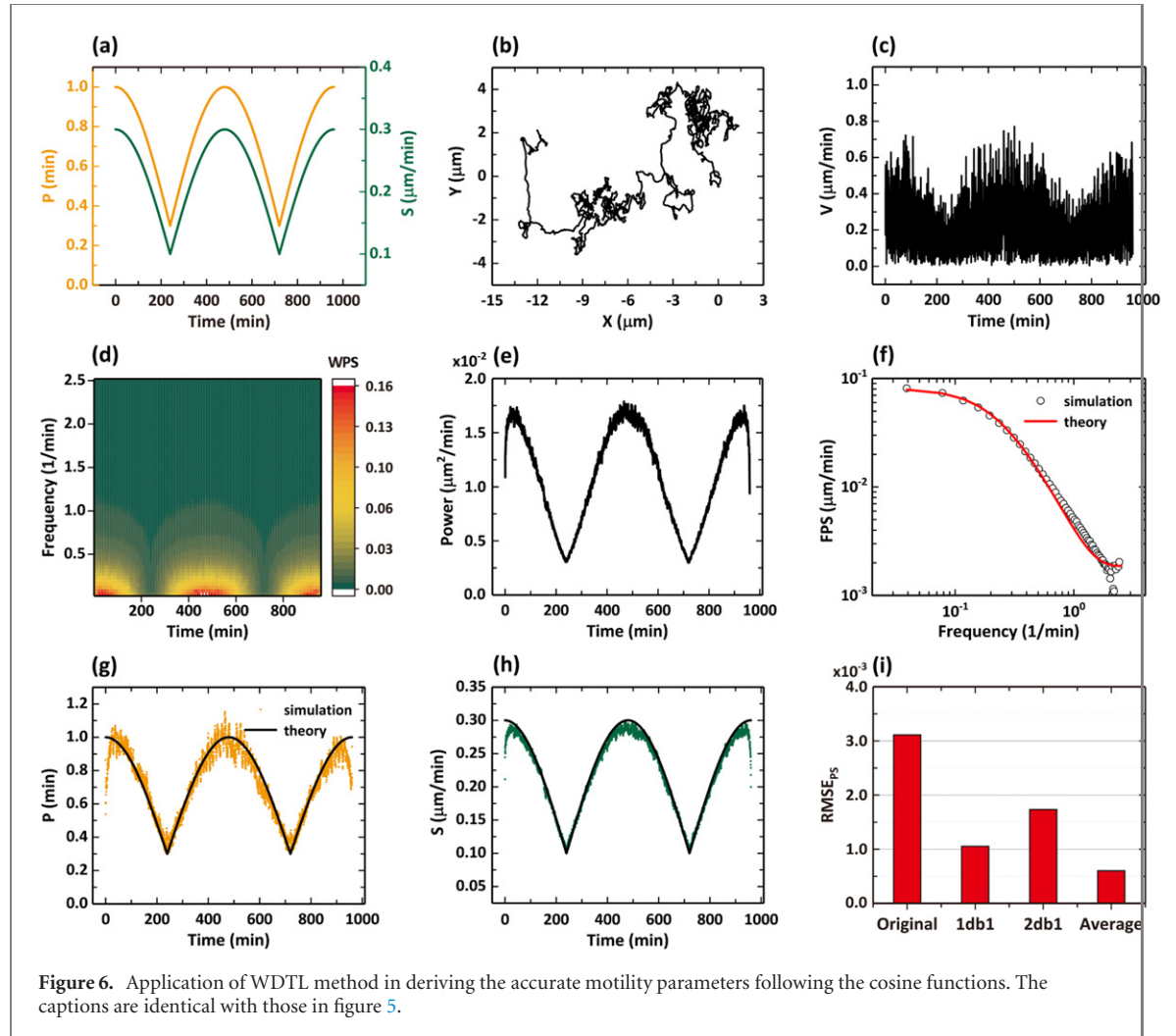


Figure 6. Application of WDTL method in deriving the accurate motility parameters following the cosine functions. The captions are identical with those in figure 5.

Table 1. The changing rates of persistence time and migration speed.

Quantities	Units	Group No.						
		1	2	3	4	5	6	7
K_p	$*(10^{-4})$	3.125	6.250	9.375	12.500	15.625	18.750	21.875
P_0	min	0.3	0.3	0.3	0.3	0.3	0.3	0.3
P_T	min	0.6	0.9	1.2	1.5	1.8	2.1	2.4
K_S	$*(10^{-4})$	2.083	4.167	6.250	8.333	10.417	12.500	14.500
S_0	$\mu\text{m min}^{-1}$	0.1	0.1	0.1	0.1	0.1	0.1	0.1
S_T	$\mu\text{m min}^{-1}$	0.3	0.5	0.7	0.9	1.1	1.3	1.5
K_{PS}	$*(10^{-4})$	2.604	5.209	7.813	10.417	13.021	15.625	18.188

and 3. Further, we employ the WDTL to derive the time-dependent motility parameters, the averaged results are shown in figures 5(g) and (h). It is noticeable that the final values are consistent well with the theoretical values in figure 5(a). Figure 5(i) compares overall RMSE_{PS} of the fitted parameters corresponding to the four denoising cases, which also illustrates that the average shows a higher performance in deriving the time-dependent motility parameters.

3.4.2. Dependency defined by cosine functions

The time-dependent functions for the second example are given by

$$P(t) = A_p \cdot \text{abs} [\cos(2\pi \cdot t / T_p)] + P_0, \quad (26)$$

$$S(t) = A_s \cdot \text{abs} [\cos(2\pi \cdot t / T_p)] + S_0, \quad (27)$$

where A_p, A_s are amplitudes, and T_p is the period of the cosine. The detail values are shown in figure 6(a).

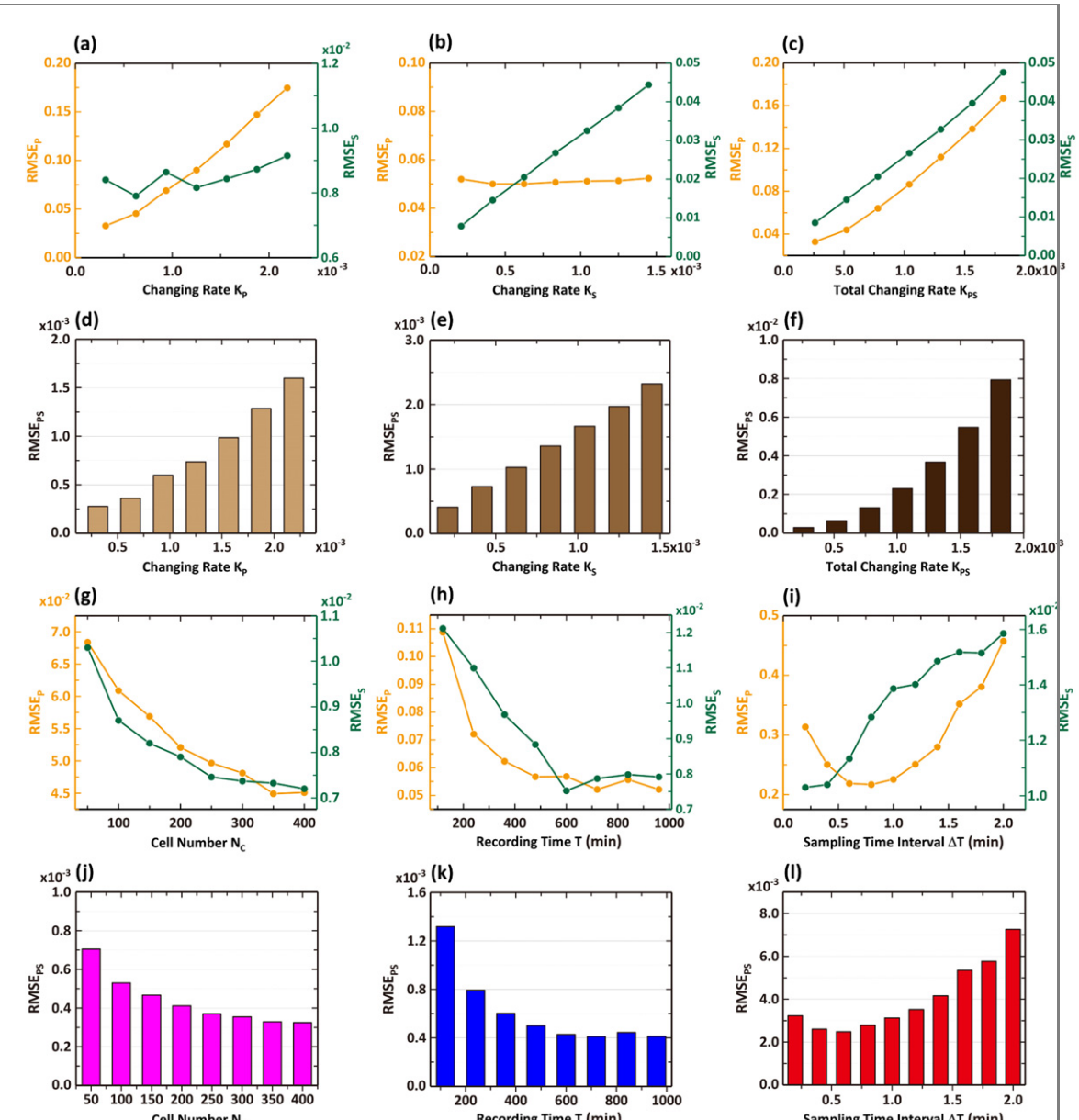


Figure 7. The effects of several factors on the performance of WDTL. (a)–(f) The effects of the changing rates of motility parameters. (a) The RMSE of the fitted persistence time P and migration speed S as functions of the changing rates K_p . The orange denotes RMSE_P of the fitted P , while the green does the RMSE_S of the fitted S . (d) The overall RMSE_{ps} as a function of the changing rates K_p . The captions of (b) and (e) are identical with those for (a) and (d), but for the changing rates K_s . (c) and (f) The RMSE_P and RMSE_S as functions of the overall changing rates K_{ps} obtained by averaging the K_p and K_s . (g) and (j) The RMSE as functions of the number of recorded cells N_c . (h) and (k) The RMSE as functions of the total recording time T for individual trajectories. (i) and (l) The RMSE as functions of the sampling time interval ΔT .

Different from the linear and quadratic functions, the above functions not only contain the enhancement of ICSP/ECM, but also the hindrance. Therefore, the cosine function provide a more realistic description of the real situations with complex time-varying properties. The corresponding results are shown in figure 6. Figures 6(g)–(i) also show the advantage of the average, which contributes to deriving the parameters reflecting the cosine dependencies.

Thus, we conclude that the WDTL can derive more accurate motility parameters from migration velocities and further mirror the real-time changing ICSP/ECM, which is also verified as a powerful analytical tool for cell motility.

3.5. The effects of several factors on the performance of WDTL

We develop a robust and accurate approach (WDTL) to deriving the time-dependent motility parameters for different time-dependent functions. In order to further understand the limitations of WDTL, we continue to investigate the performance of WDTL under the influences of more factors based on control variable and the linear functions, including the changing rates of motility parameters (K_p , K_s and K_{ps}), the number of the recorded cells (N_c), the total recording time for individual trajectories (T), and the sampling time interval (ΔT).

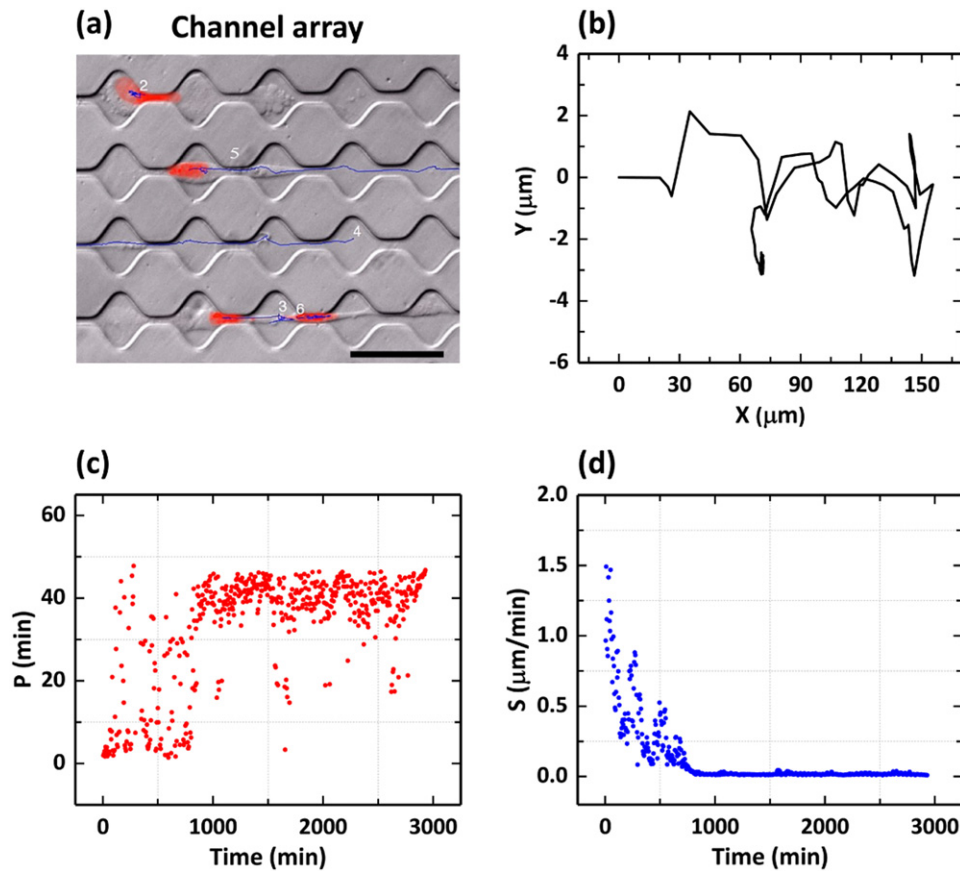


Figure 8. The time-dependent motility parameters of cell migration in micro-structural channel array. (a) Primary breast cancer cells (MDA-MB-231) migration in micro-structure containing chambers and channels. For tracking cell's position, cell nuclei are stained with Hoechst and shown in red. The scale bar is 50 μm . (b) Single migration trajectory for cell numbered '5'. The time interval between two frames is 5 min. (c) The time-dependent persistence time P for cell migration shown in (b). (d) The time-dependent migration speed S for cell migration shown in (b). The data (b) and image (a) are reproduced from Refs. [63] with permissions, respectively. Reproduced from [64]. CC BY 4.0.

In the previous sections, we only study the performances of WDTL in the cases of three time-dependent functions, which are generally not sufficient to analyze the effects of various changing rates. Thus, we define several different changing rates (see table 1), to study the effects of ICSP/ECM on the accuracy of fitting parameters. For simplicity, we again introduce linear functions [cf equations (2) and (3)], the corresponding quantities are computed and listed in table 1. The indexes K_P and K_S quantify the changing rates of parameters P and S , respectively, while the K_{PS} does the overall changing rates obtained from the average of the K_P and K_S .

Figures 7(a)–(f) exhibit the detail results. When only increasing K_P from 3.125×10^{-4} to 21.875×10^{-4} and keeping $K_S 2.083 \times 10^{-4}$, the RMSE_P of fitted P increase and the fitted S almost does not be affected [see figure 7(a)]. The overall RMSE_{PS} increase, as seen in figure 7(d). When increasing K_S from 2.083×10^{-4} to 14.5×10^{-4} and

keeping $K_P 7.292 \times 10^{-4}$, only the RMSE_S of fitted S increase [see figure 7(b)]. The overall RMSE_{PS} also increase [see figure 7(e)]. If we increase the K_P and K_S simultaneously, both the RMSE (RMSE_P and RMSE_S) of P and S increase, as seen in figures 7(c) and (f).

Inversely, we find the overall RMSE_{PS} decrease when increasing the number of the recorded cells [see figures 7(g) and (j)] or increasing the total recording time for individual trajectories [see figures 7(h) and (k)]. When keeping the total recording time $T = 960$ min constant but increasing the sampling time interval ΔT from 0.2 min to 2.0 min, the overall RMSE_{PS} first decrease and then increase [see figures 7(i) and (l)].

We conclude that the slowly changing motility parameters (ICSP/ECM) (~ 0), more recorded cells (> 250), longer recording time (> 600 min) and suitable sampling time interval (~ 0.6 min) will contribute to a better performance of our approach in fitting the time-dependent motility parameters.

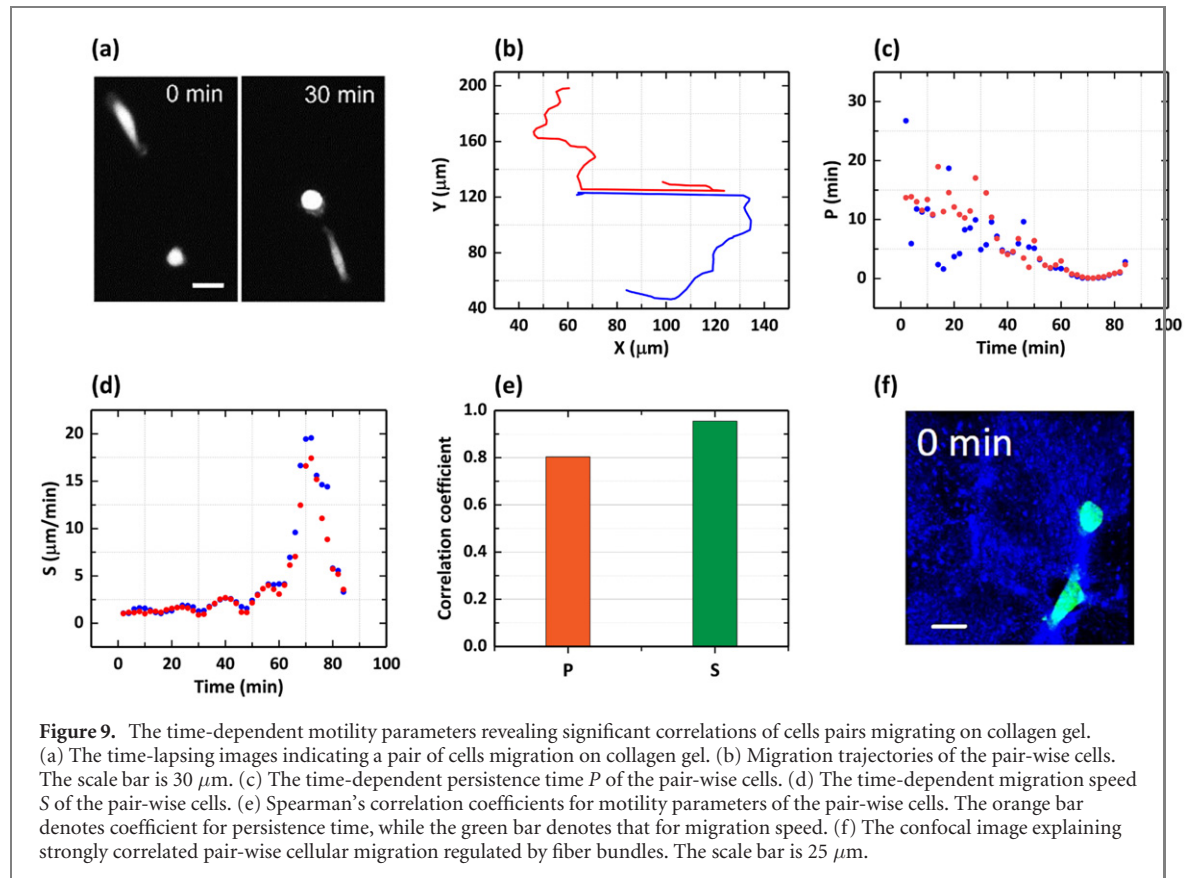


Figure 9. The time-dependent motility parameters revealing significant correlations of cells pairs migrating on collagen gel. (a) The time-lapsing images indicating a pair of cells migration on collagen gel. (b) Migration trajectories of the pair-wise cells. The scale bar is $30 \mu\text{m}$. (c) The time-dependent persistence time P of the pair-wise cells. (d) The time-dependent migration speed S of the pair-wise cells. (e) Spearman's correlation coefficients for motility parameters of the pair-wise cells. The orange bar denotes coefficient for persistence time, while the green bar denotes that for migration speed. (f) The confocal image explaining strongly correlated pair-wise cellular migration regulated by fiber bundles. The scale bar is $25 \mu\text{m}$.

4. Extracting the time-dependent motility parameters for *in vitro* cell migration regulated by complex microenvironment

4.1. The time-dependent motility parameters of cell migration in micro-structural channel array
 In section 3, we develop an approach to derive the time-varying motility parameters and further analyze the effects of several factors on this approach. Here, in order to illustrate experimentally the utility of this approach, we continue to extract the time-dependent motility parameters of *in vitro* cell migration. Firstly, we obtain the corresponding experimental data [63] of cell migration in a micro-structural channel array containing chambers and channels and primary breast cancer cells (MDA-MB-231) migrate through the array. For accurately tracking the cells, cell nuclei are stained with Hoechst and shown in red, as seen in figure 8(a). Here, we plot the migration trajectory of cell numbered '5', which contains 590 frames [see figure 8(b)]. Then, we extract the time-dependent motility parameters, using the WDTL method, as shown in figures 8(c) and (d).

In figure 8(c), the time-dependent persistence time exhibits many 'irregular' values, which are mainly the consequence of motility noises, e.g. the intrinsic noise and the positioning noise. Nevertheless, the time-dependent persistence time still shows an obvious characteristics, i.e. the

persistence time possesses a smaller value in the interval 0–800 min, while possesses a greater value in the interval 800–3000 min, which mean that cell first migrates in a more random manner, and then in a more persistent manner. Different from the characteristics of the time-dependent persistence time, the time-dependent migration speed S gradually decreases with time lapsing [see figure 8(d)]. The results above illustrate that the WDTL method is efficient in studying the time-dependent characteristics of cell migration in confined environment.

4.2. The time-dependent motility parameters revealing strong correlation between cell pairs regulated by remodeled collagen fiber bundles

To further demonstrate the utility of our approach, we obtain *in vitro* migration trajectories of MCF-10A cells on 3D collagen I hydrogel with a collagen concentration 2 mg ml^{-1} and thickness of approximately 2 mm by randomly distributing the MCF-10A cells on collagen-based ECM with a low cell density 10^4 cells/cm^2 , and we record the migration trajectories in sampling time 2 min for every frame. The details of the experimental procedure were reported in references [65, 66] and will be not repeated here.

In experiment, we observe strongly correlated pair-wise migrations for cells on collagen gel, i.e. a pair of cells move quickly toward to each other, when the initial distance between the cells is roughly within ~ 80 to $120 \mu\text{m}$, as shown in figure 9(a). We further apply the WDTL method to the migration

trajectories [see figure 9(b)] of the cell pair, and the resulting motility parameters are exhibited in figures 9(c) and (d). Qualitatively, it is interesting that the time-dependent persistence time for one cell is almost identical with that for another cell, and the migration speed for the cell pair is almost identical with each other. In order to quantify the correlation between the cell pair, we calculate the Spearman's correlation coefficient for persistence time ($r = 0.80$) and migration speed ($r = 0.95$), respectively [see figure 9(e)]. Here, Spearman is chosen because the data does not satisfy the normality criteria, even after transformation. The coefficients above indicate that a strong correlation between cell pair does exist, which means that the cell pair possesses the similar migration characteristics.

In order to analyze the mechanism underlying the strong correlations between cell pairs, we subsequently obtain the confocal image [see figure 9(f)], which clearly indicates that a pair of cells migrate toward to each other, along the collagen fiber bundle. The correlations between cell-cell, cell-fiber are mainly due to the dynamically re-arranged collagen bundles between the two migrating cells. Recent studies suggested that the remodeling of collagen fibers is mainly due to the active tensile forces generated by the migrating cells, and the bundles bridging the two cells typically carry tensile forces which in turn regulate the cell migration and lead to the observed strongly correlated migration [31, 33, 65, 67, 68].

5. Conclusions

Cell migration, which is of importance for the normal development of organisms and cancer metastasis, and is affected strictly by ICSP and ECM. In this paper, we develop an approach (WDTL) to analyze the time-varying characteristics of cell migration, namely deriving the time-dependent motility parameters to reflect the changes of ICSP/ECM with time to some extent.

As a result, the cell motility parameters are the functions of time due to the influences of ICSP/ECM, in the TPRW. Based on trajectories simulated by TPRW model, we calculate MSD, VAC and FPS and further derive three sets of motility parameters from the fits to the corresponding physical quantities. Although the three quantities can derive three sets of motility parameters, all of them only quantify the overall averaged cell migration capability instead of the time-dependent characteristics. We then introduce the WT to compute the local wavelet power spectrum at each moment and obtain the time-dependent motility parameters by employing the LPS. However, the fitted results only roughly reflect the time-varying motility parameters with large deviations from the time-dependent functions. In order to improve the accuracy of fitting motility parameters, we apply WD based on 1db1 and

2db1 to filter the migration velocities before implementing the WT. The results show clearly that the averaged parameters based on 1db1 and 2db1 can significantly decrease the errors between the fitted and the theoretical motility parameters, mirroring the time-dependent functions.

In order to verify our approach, we further analyze the cases described by quadratic and cosine functions, the results show that the approach still exhibits higher performance in fitting motility parameters. In addition, we continue to study the effects of several factors on the performances of WDTL, for instance, the changing rates of motility parameters, the number of the recorded cells, the total recording time for individual trajectories and the sampling time interval. The studies figure out the limitations of the WDTL developed, which also provide a guidance when processing the cell migration in *Lab*. Finally, we also employ our approach to experimental data of *in vitro* cell migration, including primary breast cancer cells migration through a micro-structural channel array and MCF-10A cells migration on collagen gel. The analysis shows that our approach can be as a powerful tool to derive accurately the time-dependent motility parameters, and further analyze the time-dependent characteristics of cell migration.

Data availability

The data supporting the results in this paper are available from the corresponding authors upon request.

Conflict of interest

The authors declare that they have no conflict of interest.

Acknowledgments

We thank Ben Fabry, Christoph Mark, Claus Metzner and Lena Lautscham for providing experimental data concerning channel arrays. YJ thanks the support from Arizona State University during his sabbatical leave. This research was supported by the National Natural Science Foundation of China (Grant Nos. 11974066, 11674043, 11675134, 11874310), the Fundamental Research Funds for the Central Universities (Grant No. 2019CDYGYB007), the Natural Science Foundation of Chongqing, China (Grant No. cstc2019jcyj-msxmX0477, cstc2018jcyjA3679), and the Capital Health Development Research Project, China (Grant No. 2020-2-2072).

ORCID iDs

Yanping Liu  <https://orcid.org/0000-0002-0768-1190>

Yang Jiao  <https://orcid.org/0000-0001-6501-8787>
Liyu Liu  <https://orcid.org/0000-0001-9784-8240>

References

- [1] Vicente-Manzanares M and Horwitz A R 2011 *Cell Migration: An Overview (Methods in Molecular Biology)* vol 769 (Clifton, N.J.) p 1
- [2] Cyster J G 2003 Lymphoid organ development and cell migration *Immunological Rev.* **195** 5
- [3] Tremel A, Cai A, Tirtaatmadja N, Hughes B D, Stevens G W, Landman K A and O'Connor A J 2009 Cell migration and proliferation during monolayer formation and wound healing *Chem. Eng. Sci.* **64** 247
- [4] Takakura N, Watanabe T, Suenobu S, Yamada Y, Noda T, Ito Y, Satake M and Suda T 2000 A role for hematopoietic stem cells in promoting angiogenesis *Cell* **102** 199
- [5] Friedl P and Alexander S 2011 Cancer invasion and the microenvironment: plasticity and reciprocity *Cell* **147** 992
- [6] Dang I et al 2013 Inhibitory signalling to the Arp2/3 complex steers cell migration *Nature* **503** 281
- [7] Polacheck D J, Zervantakis I K and Kamm R D 2013 Tumor cell migration in complex microenvironments *Cell. Mol. Life Sci.* **70** 1335
- [8] Kim J, Zheng Y, Alabdai A A, Nan H, Tian J, Jiao Y and Sun B 2020 Geometric dependence of 3D collective cancer invasion *Biophys. J.* **118** 1177
- [9] Gupta G P and Massagué J 2006 Cancer metastasis: building a framework *Cell* **127** 679
- [10] Jemal A, Siegel R, Xu J and Ward E 2010 Cancer statistics: CA: A Cancer J. Clinicians **60** 277
- [11] Novikova E A, Raab M, Discher D E and Storm C 2017 Persistence-driven durotaxis: generic, directed motility in rigidity gradients *Phys. Rev. Lett.* **118** 078103
- [12] Lo C-M, Wang H-B, Dembo M and Wang Y-l 2000 Cell movement is guided by the rigidity of the substrate *Biophys. J.* **79** 144
- [13] Park J, Kim D-H, Kim H-N, Wang C J, Kwak M K, Hur E, Suh K-Y, An S S and Levchenko A 2016 Directed migration of cancer cells guided by the graded texture of the underlying matrix *Nat. Mater.* **15** 792
- [14] Zhu J, Liang L, Jiao Y, Liu L and Alliante U S-C P S-O 2015 Enhanced invasion of metastatic cancer cells via extracellular matrix interface *Plos One* **10** e0118058 UNSP
- [15] Han W et al 2016 Scavenging nucleic acid debris to combat autoimmunity and infectious disease *Proc. Natl Acad. Sci. USA* **113** 11208
- [16] Weiss G H 2002 Some applications of persistent random walks and the telegrapher's equation *Physica A* **311** 381
- [17] Li L, Cox E C and Flyvbjerg H 2011 Dicty dynamics: dictyostelium motility as persistent random motion *Phys. Biol.* **8** 046006
- [18] Sadjadi Z, Shaebani M R, Rieger H and Santen L 2015 Persistent-random-walk approach to anomalous transport of self-propelled particles *Phys. Rev. E* **91** 062715
- [19] Lemons D S and Gythiel A 1997 Paul Langevin's 1908 paper on the theory of Brownian motion Sur la théorie du mouvement Brownien *Am. J. Phys.* **65** 1079
- [20] Schienbein M and Gruler H 1993 Langevin equation, Fokker–Planck equation and cell migration *Bull. Math. Biol.* **55** 585
- [21] Stokes C L, Lauffenburger D A and Williams S K 1991 Migration of individual microvessel endothelial cells: stochastic model and parameter measurement *J. Cell Sci.* **99** 419
- [22] Codling E A, Plank M J and Benhamou S 2008 Random walk models in biology *J. R. Soc. Interface.* **5** 813
- [23] Li L, Norrelykke S F and Cox E C 2008 Persistent cell motion in the absence of external signals: a search strategy for eukaryotic cells *Plos One* **3** e2093
- [24] Harris T H et al 2012 Generalized Lévy walks and the role of chemokines in migration of effector CD8+ T cells *Nature* **486** 545
- [25] Shenderov A D and Sheetz M P 1997 Inversely correlated cycles in speed and turning in an ameba: an oscillatory model of cell locomotion *Biophys. J.* **72** 2382
- [26] Vestergaard C L, Pedersen J N, Mortensen K I and Flyvbjerg H 2015 Estimation of motility parameters from trajectory data *Eur. Phys. J. Spec. Top.* **224** 1151
- [27] Vestergaard C L, Blainey P C and Flyvbjerg H 2014 Optimal estimation of diffusion coefficients from single-particle trajectories *Phys. Rev. E* **89** 022726
- [28] Gorelik R and Gautreau A 2014 Quantitative and unbiased analysis of directional persistence in cell migration *Nat. Protocols* **9** 1931
- [29] Liu Y-P, Zhang X-C, Wu Y-L, Liu W, Li X, Liu R-C, Liu L-Y and Shuai J-W 2017 Derivation of persistent time for anisotropic migration of cells *Chin. Phys. B* **26** 128707
- [30] Liu Y-P, Li X, Qu J, Gao X-J, He Q-Z, Liu L-Y, Liu R-C and Shuai J-W 2020 Motile parameters of cell migration in anisotropic environment derived by speed power spectrum fitting with double exponential decay *Front. Phys.* **15** 13602
- [31] Liang L, Jones C, Chen S H, Sun B and Jiao Y 2016 Heterogeneous force network in 3D cellularized collagen networks *2016 Phys. Biol.* **13** 066001
- [32] Nan H Q, Liang L, Chen G, Liu L Y, Liu R C and Jiao Y 2018 Realizations of highly heterogeneous collagen networks via stochastic reconstruction for micromechanical analysis of tumor cell invasion *Phys. Rev. E* **97** 033311
- [33] Zheng Y et al 2019 Are gravitating magnetic monopoles stable? *Phys. Rev. E* **100** 043303
- [34] Bergman A and Zygourakis K 1999 Migration of lymphocytes on fibronectin-coated surfaces: temporal evolution of migratory parameters *Biomaterials* **20** 2235
- [35] Pedersen J N, Li L, Grdinariu C, Austin R H, Cox E C and Flyvbjerg H 2016 How to connect time-lapse recorded trajectories of motile microorganisms with dynamical models in continuous time *Phys. Rev. E* **94** 062401
- [36] Wu P-H, Giri A, Sun S X and Wirtz D 2014 Three-dimensional cell migration does not follow a random walk *Proc. Natl Acad. Sci. USA* **111** 3949
- [37] Maiuri P et al 2015 Actin flows mediate a universal coupling between cell speed and cell persistence *Cell* **161** 374
- [38] Uhlenbeck G E and Ornstein S 1930 On the theory of the Brownian motion *Phys. Rev.* **36** 823
- [39] Wu P-H, Giri A and Wirtz D 2015 Statistical analysis of cell migration in 3D using the anisotropic persistent random walk model *Nat. Protocols* **10**
- [40] Cohen L 1998 Generalization of the Wiener–Khinchin theorem *IEEE Signal Process. Lett.* **5** 292
- [41] Leibovich N, Dechant A, Lutz E and Barkai E 2016 Aging Wiener–Khinchin theorem and critical exponents of 1/β (beta) noise *Phys. Rev. E* **94** 052130
- [42] Morlet J, Arens G, Fourneau E and Glard D 1982 Wave propagation and sampling theory-part I: complex signal and scattering in multilayered media *Geophysics* **47** 203
- [43] Morlet J, Arens G, Fourneau E and Giard D 1982 Wave propagation and sampling theory-part II: sampling theory and complex waves *Geophysics* **47** 222
- [44] Goupillaud P, Grossmann A and Morlet J 1984 Cycle-octave and related transforms in seismic signal analysis *Geoexploration* **23** 85
- [45] Grossmann A and Morlet J 1984 Decomposition of Hardy functions into square integrable wavelets of constant shape *SIAM J. Math. Anal.* **15** 723
- [46] Flandrin P 1992 Wavelet analysis and synthesis of fractional Brownian motion *IEEE Trans. Inf. Theory* **38** 910
- [47] Kumar P and Foufoula-Georgiou E 1997 Wavelet analysis for geophysical applications *Rev. Geophys.* **35** 385
- [48] Kaiser G and Hudgin L H J P T 1995 Continuous Wavelet Transforms A Friendly Guide to Wavelets 48 (New York: Birkhäuser) pp 60–77
- [49] Torrence C and Compo G P 1998 A practical guide to wavelet analysis *Bull. Am. Meteorol. Soc.* **79** 61
- [50] Daubechies I 1992 Ten Lectures On Wavelets *Comput. Phys.* **6** 697
- [51] Lau K M and Weng H 1995 Climate signal detection using wavelet transform: How to make a time series sing *Bull. Am. Meteorol. Soc.* **76** 2391

- [52] Farge M 1992 WAVELET TRANSFORMS AND THEIR APPLICATIONS TO TURBULENCE *Annu. Rev. Fluid Mech.* **24** 395
- [53] Shyu H C and Sun Y S 2002 Construction of a Morlet wavelet power spectrum *Multidimens. Syst. Signal Process.* **13** 101
- [54] Gilman D L, Fuglister F J and Mitchell J M 1963 ON THE POWER SPECTRUM OF RED NOISE *J. Atmos. Sci.* **20** 182
- [55] Percival D P 1995 ON ESTIMATION OF THE WAVELET VARIANCE *Biometrika* **82** 619
- [56] Soltani S 2002 On the use of the wavelet decomposition for time series prediction *Neurocomputing* **48** 267
- [57] Mallat S G 1989 A THEORY FOR MULTIRESOLUTION SIGNAL DECOMPOSITION - THE WAVELET REPRESENTATION *IEEE Trans. Pattern Anal. Mach. Intell.* **11** 674
- [58] Daubechies I 1990 THE WAVELET TRANSFORM, TIME-FREQUENCY LOCALIZATION AND SIGNAL ANALYSIS *IEEE Trans. Inf. Theory* **36** 961
- [59] Subramani P, Sahu R and Verma S 2006 Feature selection using Haar wavelet power spectrum *BMC Bioinformatics* **7** 432
- [60] Ramsey F L and Schafer D W 2002 *The statistical sleuth : a course in methods of data analysis* 3rd (Belmont, CA: Duxbury Press) 760
- [61] Cattani C 2004 Haar wavelet-based technique for sharp jumps classification *Math. Comput. Modelling* **39** 255
- [62] Jie L and Xuan-Hao D 2007 Denoising for Haar Wavelet Discrete and Its Application *J. Guangxi Acad. Sci.*
- [63] Lautscham L A *et al* 2015 Migration in Confined 3D Environments Is Determined by a Combination of Adhesiveness, Nuclear Volume, Contractility, and Cell Stiffness *Biophys. J.* **109** 900
- [64] Metzner C, Mark C, Steinwachs J, Lautscham L, Stadler F and Fabry B 2015 Superstatistical analysis and modelling of heterogeneous random walks *Nat. Commun.* **6** 7516
- [65] Fan Q *et al* 2021 Dynamically re-organized collagen fiber bundles transmit mechanical signals and induce strongly correlated cell migration and self-organization *Angew. Chem., Int. Ed. Engl.*
- [66] Zheng Y, Fan Q H, Eddy C Z, Wang X C, Sun B, Ye F F and Jiao Y 2020 Modeling multicellular dynamics regulated by extracellular-matrix-mediated mechanical communication via active particles with polarized effective attraction *Phys. Rev. E* **102** 052409
- [67] Nan H Q, Zheng Y, Lin Y H H, Chen S H, Eddy C Z, Tian J X, Xu W X, Sun B and Jiao Y 2019 Absorbing-active transition in a multi-cellular system regulated by a dynamic force network *Soft Matter* **15** 6938
- [68] Chen S H, Xu W X, Kim J H, Nan H Q, Zheng Y, Sun B and Jiao Y 2019 Novel inverse finite-element formulation for reconstruction of relative local stiffness in heterogeneous extra-cellular matrix and traction forces on active cells *Phys. Biol.* **16** 036002